International Journal of Applied Earth Observation and Geoinformation 26 (2014) 350–362

Contents lists available at ScienceDirect

International Journal of Applied Earth Observation and Geoinformation

journal homepage: www.elsevier.com/locate/jag

Mapping spatio-temporal flood inundation dynamics at large river basin scale using time-series flow data and MODIS imagery

Chang Huang[a,b,*], Yun Chen[b], Jianping Wu[a]

[a] Key laboratory of Geographic Information Science (Ministry of Education), East China Normal University, Shanghai 200241, China
[b] CSIRO Land and Water, Canberra ACT 2601, Australia

ARTICLE INFO

Article history:
Received 1 February 2013
Accepted 9 September 2013

Keywords:
Observed flow
Annual flood series
MODIS
OWL
Inundation frequency
Inundation probability

ABSTRACT

Flood inundation is crucial to the survival and prosperity of flora and fauna communities in floodplain and wetland ecosystems. This study tried to map flood inundation characteristics in the Murray-Darling Basin, Australia, utilizing hydrological and remotely sensed data. It integrated river flow time series and Moderate Resolution Imaging Spectroradiometer (MODIS) images to map inundation dynamics over the study area on both temporal and spatial dimensions. Flow data were analyzed to derive flow peaks and Annual Exceedance Probabilities (AEPs) using the annual flood series method. The peaks were linked with MODIS images for inundation detection. Ten annual maximum inundation maps were generated for water years 2001–2010, which were then overlaid to derive an inundation frequency map. AEPs were also combined with the annual maximum inundation maps to derive an inundation probability map. The resultant maps revealed spatial and temporal patterns of flood inundation in the basin, which will benefit ecological and environmental studies when considering response of floodplain and wetland ecosystems to flood inundation.

1. Introduction

Floods are important water sources for many riparian plants in arid and semi-arid regions to survive and flourish. They particularly play a critical role in sustaining ecosystems in river corridors and in maintaining biodiversity of floodplains and wetlands (APFM, 2006). Periodic flooding is essential to the well-being of flora and fauna communities along the rivers and around the lakes, whose living conditions are closely related to flood inundation characteristics such as extent and frequency. Therefore, mapping flood inundation at both spatial and temporal scales is helpful for monitoring the sustainability of ecosystems.

In situ gauge data are the backbone of the current understanding of surface water dynamics (Alsdorf et al., 2007), and have been essential for fundamental flood research. Although river discharge data have been used for flood frequency analysis in many studies (Saf, 2009; Shi et al., 2010; Seckin et al., 2011), and have strengths in quantifying the temporal pattern of water movement (discharge) within river and stream channels, they provide comparatively little information about the spatial dynamics of surface water extent in floodplains and wetlands during periods of flood inundation (Papa et al., 2008). Research needs have been requiring a move beyond the point-based observations provided by gauges to basin-wide measurements of water distributions (Alsdorf and Lettenmaier, 2003). Several studies (Frank et al., 2001; Dutta et al., 2007; Bates et al., 2010) have used hydraulic models to estimate the dynamics of surface water for small areas based on observed gauge data. Some also have developed hydrodynamic models to map flood inundation at large scale or even global scale (Paz et al., 2011; Wilson et al., 2007; Yamazaki et al., 2011; Pappenberger et al., 2012; Westerhoff et al., 2013; Neal et al., 2012) using low resolution digital elevation models (DEMs). However, difficulties in modeling inundation across large areas may be encountered due to data scarcity and the complexity of establishing spatial connections between main channel and floodplain. In addition, the computational cost is high for fine time step or long term period analysis. Remote sensing techniques have demonstrated advanced capabilities to map surface water features and to monitor surface water dynamics (Ji et al., 2009). They have been combined with hydraulic models using assimilation methods to map inundation dynamics in a few studies (Giustarini et al., 2011; Mason et al., 2012; Garcia-Pintado et al., 2013). Inundation extent derived from remote sensing has been proven to be closely correlated with ground measurements of river discharge (Smith et al., 1996; Vorosmarty et al., 1996; Smith, 1997; Benke et al., 2000; Frazier et al., 2003; Overton, 2005; Frazier and Page, 2009). These studies suggest that the combination of gauge

* Corresponding author at: Key Laboratory of Geographic Information Science (Ministry of Education), East China Normal University, Shanghai 200241, China. Tel.: +86 21 54341173.
E-mail addresses: ahuang.86@163.com, chang.huang@csiro.au, chaunceyhuang@gmail.com (C. Huang), yun.chen@csiro.au (Y. Chen), jpwu@geo.ecnu.edu.cn (J. Wu).

0303-2434/$ – see front matter © 2013 Elsevier B.V. All rights reserved.
http://dx.doi.org/10.1016/j.jag.2013.09.002

observations and remotely sensed detection could offer a practical way to map spatial and temporal inundation dynamics in broad areas such as large river basins.

There are generally two types of remote sensors that are suitable for inundation detection, microwave sensors and optical sensors. Microwave sensors such as Synthetic Aperture Radar (SAR; Matgen et al., 2007; Di Baldassarre et al., 2011) have been proven to be useful in mapping flood under all weather conditions as they can penetrate clouds. Images from optical remote sensors, such as Landsat Multispectral Scanner (MSS), Thematic Mapper/Enhanced Thematic Mapper Plus (TM/ETM+; Rango and Salomonson, 1974; Bhavsar, 1984; Wang et al., 2002) and SPOT (Blasco et al., 1992), are more common and more easily acquired. Other relatively coarse resolution images have also been used in classifying flooded areas, such as Advanced Very High Resolution Radiometer (AVHRR; Islam and Sado, 2000a,b) and Moderate Resolution Imaging Spectroradiometer (MODIS; Islam et al., 2010; Kwak et al., 2011; Brakenridge, 2013; Chen et al., 2013). Although these images have lower spatial resolutions and are frequently contaminated by cloud cover, their merit lies in their higher temporal resolutions (Huang et al., 2013). These qualities make them well-suited to spatio-temporal analysis on flood inundation for large river basins (Gumbricht et al., 2004; Sakamoto et al., 2007; Westra and De Wulf, 2009; Li et al., 2011; Huang et al., 2012a,b).

For optical sensors such as MODIS, the basis for open water delineation is to make use of their infrared bands, because these bands are strongly absorbed by water while highly reflected by vegetation and dry soils. Density slicing or image classification methods are commonly applied on these bands to extract water bodies. Indices have been derived to enhance the spectral difference between water and non-water for better discrimination, such as the Normalized Difference Water Index (NDWI; Gao, 1996; McFeeters, 1996; Hui et al., 2008) and the modified NDWI (mNDWI; Xu, 2006; Ordoyne and Friedl, 2008; Chen et al., 2012b; Michishita et al., 2012). A threshold of 0 is generally used to delineate water bodies. However, it is believed that manual adjustment on the threshold is always needed to achieve more accurate results (Ji et al., 2009). Guerschman et al. (2011) introduced the Open Water Likelihood (OWL) algorithm for estimating standing water from MODIS images. The OWL was developed by investigating the spectral properties of open water. It was found that the OWL provides a more accurate representation of inundation throughout the time series of images comparing with the other indices such as NDWI or mNDWI (Guerschman et al., 2011). Its performance has been tested in the Australia continent (Guerschman et al., 2011; Chen et al., 2011; Overton et al., 2011; Chen et al., 2012a,b, 2013; Huang et al., 2012a).

Remote sensing has been applied in many flood related researches for decades (Rango and Salomonson, 1974; Bhavsar, 1984; Blasco et al., 1992; Islam and Sado, 2000a; Islam et al., 2010). There are several pioneer studies that have attempted to map spatial and temporal variations of flood inundation. Sakamoto et al. (2007) investigated the temporal changes in annual flood inundation extent within the Mekong Delta using MODIS time-series imagery. Islam et al. (2010) studied spatio-temporal variations of inundation extent in 2004 and 2007 in Bangladesh. Pulvirenti et al. (2011) employed multi-temporal radar images to map flood inundation dynamics in Northern Italy. Thomas et al. (2011) mapped flood inundation frequency in the Macquarie Marshes of Australia over 28 years using Landsat images. However, these investigations examined time-series images without considering hydrological data which could make research outcomes more explicit and useful to eco-hydrological studies.

The aim of this study is to develop a methodology that can be used to map spatial and temporal dynamics of flood inundation by integrating MODIS images and observed daily flow data. The main objectives of this study are, (1) to extract annual maximum inundation extents for revealing the maximum extent inundated in each water year; (2) to map flood inundation frequency to demonstrate how often an area was inundated historically; and (3) to derive a flood probability map to indicate how likely an area may be inundated in the future.

2. Study area and data

2.1. Study area

The Murray-Darling Basin (hereinafter referred to as the Basin) is Australia's largest river basin. Within the basin, 17 large and complex floodplain wetland systems have been identified which are associated with relatively large perennial or intermittent rivers (Rogers and Ralph, 2010). Altogether, the floodplain wetlands are very extensive, covering 6% of the Basin and accounting for over 95% of all wetland areas within the inland catchments of Australia (Kingsford et al., 2004). Most rivers in the Basin run from temperate uplands on the southern and eastern margins, and drain inland toward increasingly low elevation and low relief (lowland), semi-arid to arid (dryland) depositional settings (Thoms and Sheldon, 2000; Ward et al., 2002). The wetlands in the Basin are important for many water dependent ecosystems, which require specific seasonal and inter-year flooding regimes to maintain ecological function.

There is a wide range of climate conditions in the Basin including a strong east-west rainfall gradient and a strong north-west to south-east temperature gradient. Rainfall is summer dominated in the north and winter dominated in the south. Rainfall varies considerably between years in the north-west and less so toward the south-west. Average annual rainfall from 1895 to 2006 across the Basin is 475 mm. Average annual potential evapotranspiration is about 1440 mm, which is more than three times the average annual rainfall (CSIRO, 2008). Therefore, water is a valuable resource within the Basin.

Three of the largest rivers in the Basin are the Murray River, the Darling River and the Murrumbidgee River. Usually, the Basin is considered as two parts with a northern region covering the drainage area of the Darling River, and a southern region including the drainage area of the Murray River, the Murrumbidgee River and the river basin below the confluence of the Darling River. The northern region contains many important wetlands, such as the Macquarie Marshes, the Gwydir wetlands, the Narran Lakes and the Paroo wetlands, while the southern region includes Chowilla floodplains and Lindsay-Wallpolla Islands, the Banrock wetlands and the Coorong, Lower Lakes and the Murray Mouth. Many of these wetland and lake systems require sufficient flood peaks from river channel to fill with water, which often has inter-year variability in occurrence.

The river networks and terrain of the Basin are complex, which makes the flood water dynamic quite variable across the Basin. To reflect the spatial variation in flood pulses and decrease time-lags between flow and inundation, Overton et al. (2011) (revised by Chen et al. (2012a)) mapped the Basin into small zones based on ecological and hydrological rules. Within each zone, the extent of floodplain inundation is linked to their associated rivers and inundation time-lags from flow are reduced. In this study, the 95 zones mapped by Chen et al. (2012a) were adopted. 47 of these zones are in the northern part of the Basin, and 48 in the southern. Fiver zones were excluded in this study because of lack of flow data (Fig. 1). Two sites, Narran Lakes in zone 95 and Chowilla Floodplain in zone 88, were selected from the important wetlands in the north and south of the Basin respectively, to demonstrate the inundation detection and evaluation method.

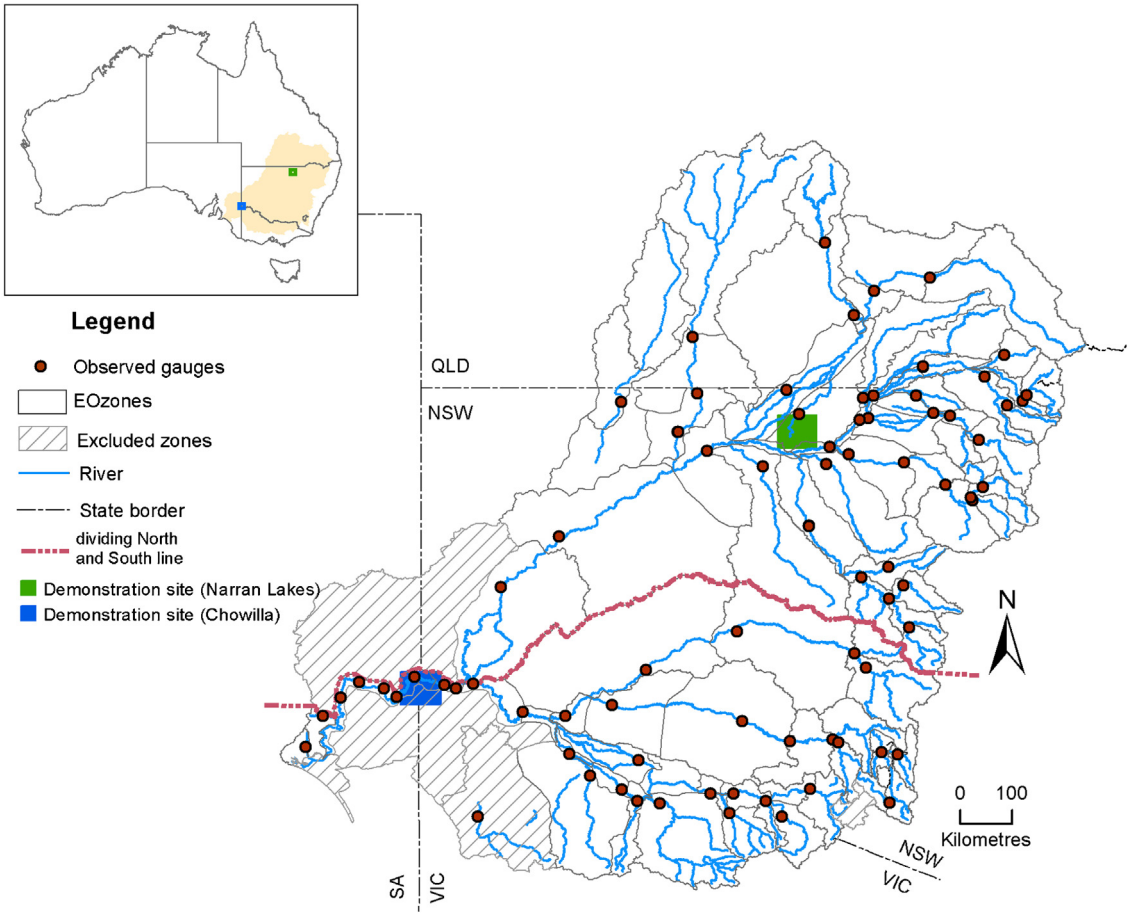

Fig. 1. Study area in eco-hydrological zones showing the delineation between the northern and southern regions, the boundaries of 95 zones, the major rivers and the demonstration sites.

2.2. Materials

2.2.1. Flow data

Observed gauge flow data were collected to define peak flows (as daily discharge in Giga Liters per day (GL/day)). Gauges were selected based on the availability and length of the flow data record to acquire at least one series of daily flow data to best represent the flow for each zone (Overton et al., 2009). Locations of all selected gauges are shown in Fig. 1. Historical flow data were extracted from the data collected by Overton et al. (2011) and Chen et al. (2012a), which are dated back to 1/1/1982. Thus, gauges have a record of 28 complete water years (from water year 1983 to 2010), as in Australia, water year is defined as from the 1st July of the preceding year to the 30th June of the current year. After checking with the flow data, there are four zones that have no related observed gauges, and one zone has observer flow data with too many missing records. Hence, these zones were excluded from the study area (Fig. 1).

2.2.2. Remotely sensed imagery

MODIS images were used for inundation detection and Landsat TM/ETM+ for evaluating the accuracy of MODIS. The MODIS data are distributed through the online Data Pool at the NASA Land Processes Distributed Active Archive Center (LP DAAC), USGS/Earth Resources Observation and Science (EROS) Center, Sioux Falls, South Dakota. In this study, time series images of MODIS Terra product "MOD09A1" from year 2000 to 2010 were used. These images are 8-day composite data at a 500 m resolution. Compositing involves compiling daily images over an eight-day period and selecting pixels of the highest quality based on a combination of low view angle, the absence of clouds or cloud shadow, and aerosol loading (USGS, 2012). In general, this process reduces interference from cloud cover and sensor aberrations, resulting in improved image quality, but the trade-offs are the possibility of missing inundation caused by rapid-changing flood events. Landsat TM/ETM+ images at 30 m resolution were acquired from USGS/EROS Center (USGS, 2011). One image for each demonstration site (Fig. 1) was acquired for evaluation of detected inundation extent on MODIS images.

3. Methodology

This study integrates hydrological observation data and remotely sensed data to map the spatial and temporal dynamics of flood inundation. The methodology consists of four components (Fig. 2), (1) flow data analysis to extract flow peaks and Annual Exceedance Probabilities (AEPs); (2) inundation detection using OWL on selected MODIS images based on flow peaks; (3) inundation evaluation using mNDWI on Landsat TM/ETM+ images; and (4) inundation mapping of annual maximum inundation, flood inundation frequency and flood probability. This method was implemented with Python scripting.

3.1. Flow data analysis

A flow peak is defined as the maximum volume flow rate passing the observed gauge. River floods are generally caused by flow peaks. Therefore, the analysis on flow peaks is also called flood

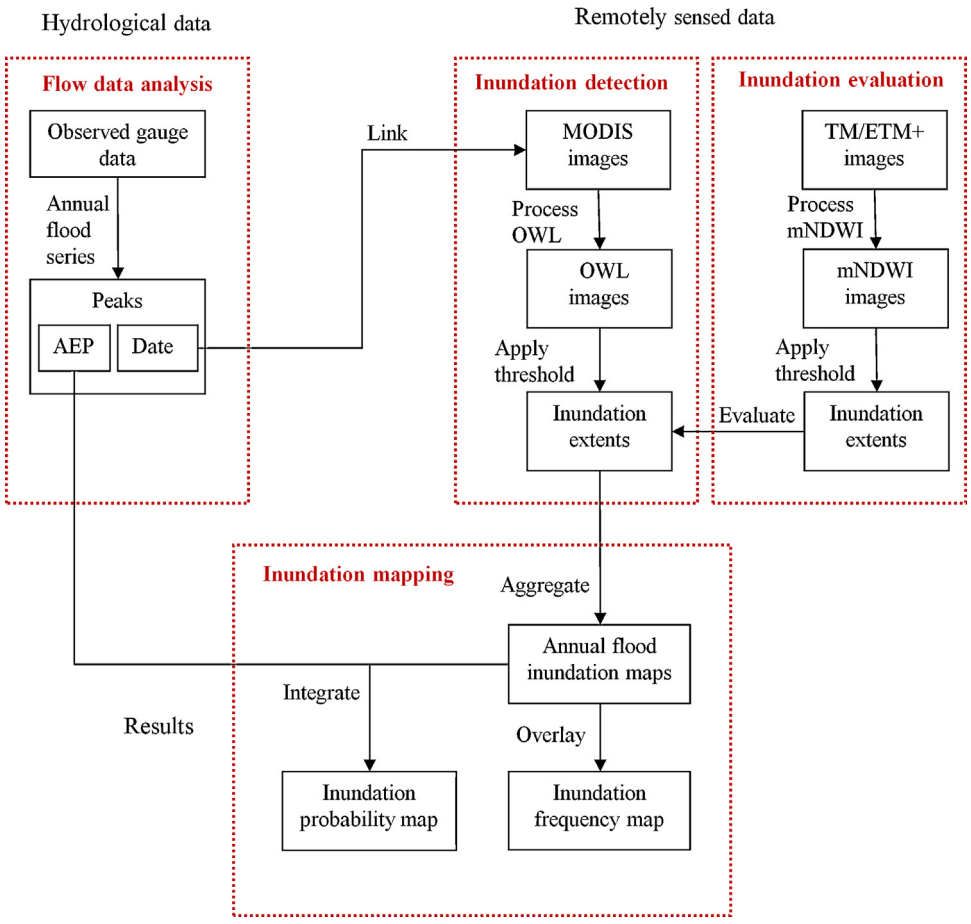

Fig. 2. Flowchart of methodology showing its four components.

frequency analysis. Flood frequency analysis was conducted using annual flood series method in this study because it retains only the largest peak for each year (Page and McElroy, 1981), which ensured that all gauges have a least one peak in each single water year for annual inundation analysis. An annual flood is defined as the highest peak discharge in a water year.

Fig. 3 shows the daily flow for Chowilla demonstration site using gauge A4260200. Peaks derived with the annual flood series method are displayed as the red diamonds. Of these, only those of water year 2001–2010 were used to link MODIS images in this study because of the availability of MODIS data.

AEPs could also be derived along with the flow peaks using the annual flood series method. AEP is the probability that a flood (flow peak) of a given size or larger will occur in any one year. AEPs could be calculated using one of the various plotting position models that have been proposed in the last decades (Gringorten, 1963; Cunnane, 1978; Kim et al., 2012). Basically, there is little difference between all these models if the sample size is large enough. Several studies have recommended Gringorten's model (Gringorten, 1963) as a suitable formula for the Gumbel distribution (Cunnane, 1978; Guo, 1990). This distribution is useful in predicting the chance that an extreme earthquake, flood or other natural disaster will occur. Assuming that flow peaks obey the Gumbel distribution, the Gringorten's model was thus adopted in this study. It is shown as

$$\mathrm{AEP} = \frac{r - 0.44}{N + 0.12} \tag{1}$$

where AEP is the annual exceedance probability; r is the rank of the annual flow peaks from largest to smallest; N is the number of years for the record length.

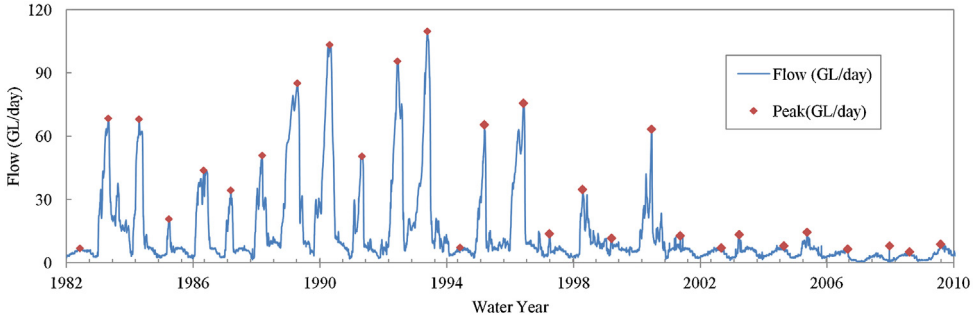

Fig. 3. Flow data and peaks of gauge A4260200 from water year 1983 to 2010.

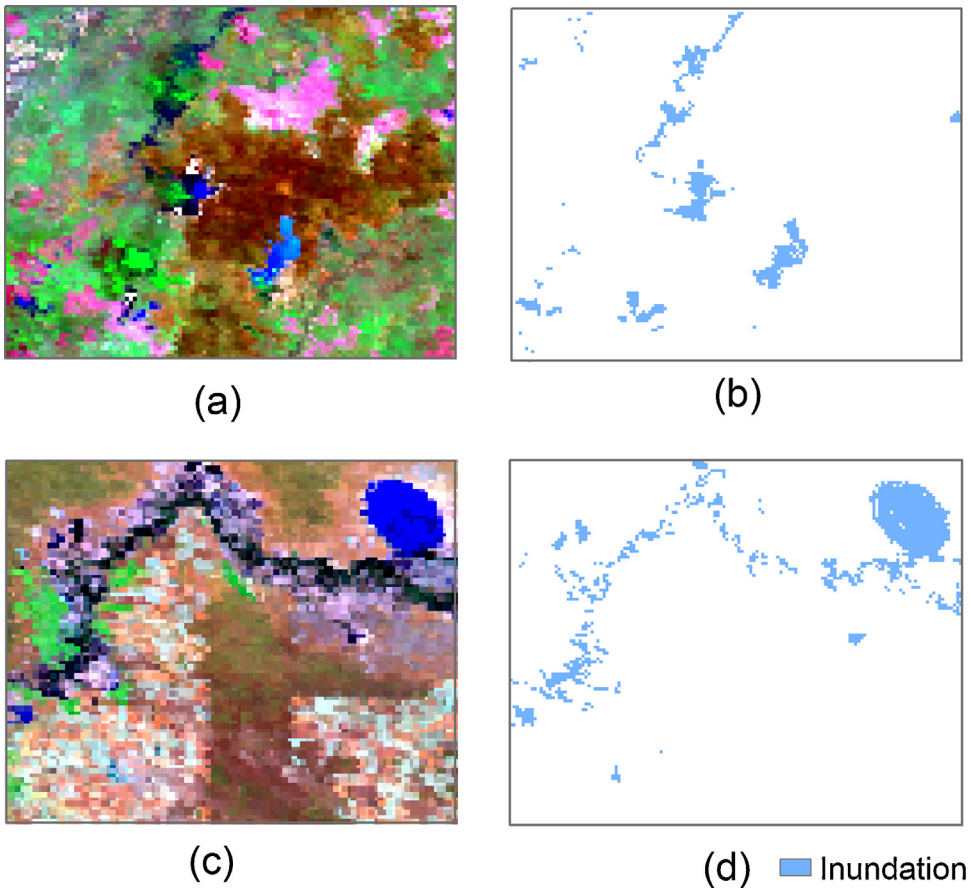

Fig. 4. (a) Color composite (R7G2B4) MODIS image (22/03/2010) of Narran Lakes; (b) inundation map with a threshold = 1 (OWL > 1) of Narran Lakes; (c) Color composite (R7G2B4) MODIS image (10/12/2000) of Chowilla; (d) inundation map with a threshold = 1 (OWL > 1) of Chowilla.

For gauge A4260200, the number of years for the available record length was 28. The AEPs of these peaks are listed in Table 1.

3.2. Inundation detection

Inundation detection was achieved using MODIS imagery where the flood inundation estimated from a single image is an instantaneous inundation condition. Since a flood event has duration, the inundation extracted by a single image rarely represents the maximum flood extent. Also, the timing of the flood peak in relation to its occurrence in the MODIS image is going to be offset by the relative gauge position within the catchment, where a zone with a gauge in the upstream section would likely have a delay between a flow and a subsequent inundation extent compared to a zone with an end-of-valley gauge which would have the corresponding inundation occurring before the flow was recorded in the gauge (Overton et al., 2009). Considering the flood duration and time lag between the gauge flow and inundation, seven images (*i.e.* 56-day period) were selected corresponding to a flow peak, with the date of the middle image closest to the peak date at the gauge.

The OWL algorithm (Guerschman et al., 2011) was adopted to map inundation on selected MODIS imagery (Fig. 4(a) and (c)). It was derived using a nonlinear logistic regression model which consists of five water-sensitive parameters. These are two Short-Wave Infrared (SWIR) bands, the Normalized Difference Vegetation Index (NDVI; Townshend and Justice, 1986), the Normalized Difference Water Index (NDWI; Gao, 1996) and the Multi-resolution Valley Bottom Flatness (MrVBF; Gallant and Dowling, 2003). It has been calibrated and optimized by Guerschman et al. (2011) based on its performance in the Australia continent. They reported that,

Table 1
Peaks and their annual exceedance probabilities (AEPs) of gauge A4260200.

Water year	Rank	Peak discharge (GL/day)	AEP (%)
1983	25	7.1	87.3
1984	6	68.7	19.8
1985	7	68.3	23.3
1986	15	20.8	51.8
1987	12	44.0	41.1
1988	14	34.6	48.2
1989	10	51.0	34.0
1990	4	85.2	12.7
1991	2	103.5	5.5
1992	11	50.7	37.6
1993	3	95.7	9.1
1994	1	109.9	2.0
1995	24	7.5	83.8
1996	8	65.5	26.9
1997	5	75.7	16.2
1998	17	13.7	58.9
1999	13	34.7	44.7
2000	20	11.6	69.6
2001	9	63.4	30.4
2002	19	12.7	66.0
2003	26	7.1	90.9
2004	18	13.3	62.4
2005	23	7.9	80.2
2006	16	14.6	55.3
2007	27	6.6	94.5
2008	22	8.1	76.7
2009	28	5.2	98.0
2010	21	8.7	73.1

Table 2
MODIS and Landsat TM/ETM+ images (subsets) used for evaluation.

Site	Date of max flow	Date of MODIS	Inundation map of MODIS	Landsat sensor	Date of TM/ETM+	Threshold for mNDWI	Inundation map of TM/ETM+
Narran	02/04/2010	22/03/2010	Fig. 4(b)	TM	23/03/2010	−0.10	Fig. 5(b)
Chowilla	11/12/2000	10/12/2000	Fig. 4(d)	ETM+	13/12/2000	−0.15	Fig. 5(d)

although it overestimated the amount of surface water in shaded slopes and also misclassified black soils as open water, it showed coherent patterns of inundation across the Murray-Darling Basin. Its merit lies in the consistent performance over image time series, which means a unique cut-off threshold on whole time series can be applied to derive coherent inundation results. The OWL index is calculated as

$$\mathrm{OWL} = \frac{1}{1+\exp(f)} \tag{2}$$

where

$$f = a_0 + \sum_{i=1}^{5} a_i x_i \tag{3}$$

and $a_0 = -3.41375620$; $a_1 = -0.000959735270$; $a_2 = 0.00417955330$; $a_3 = 14.1927990$; $a_4 = -0.430407140$; $a_5 = -0.0961932990$; x_1 = SWIR Band 6 (reflectance × 1000); x_2 = SWIR Band 7 (reflectance × 1000); x_3 = NDVI (NDVI = (Band 2 − Band 1)/(Band 2 + Band 1)); x_4 = NDWI (NDWI = (Band 2 − Band 6)/(Band 2 + Band 6)), and x_5 = MrVBF (an index derived from 9 second Shuttle Radar Topography Mission (SRTM) DEM indicating the degrees of valley bottom flatness (Gallant and Dowling, 2003)).

OWL index ranges from 0 to 100 representing the likelihood of the presence of water within a MODIS 500 m pixel (Guerschman et al., 2011). Using a suitable cut-off threshold, inundation extent can be derived from OWL images. Various thresholds were trialed with a value of 1 producing the closest agreement with the water boundaries visualized from Landsat images (Chen et al., 2013). Pixels with an OWL index great than 1 were identified as inundated pixels (Fig. 4(b) and (d)).

3.3. Inundation evaluation

Inundation extents derived by Landsat TM/ETM+ images were used as the "ground truth" to evaluate the OWL method on MODIS images as these images have a relatively higher resolution (30 m). Inundations on TM/ETM+ images were derived using mNDWI which is one of the most popular indices for inundation detection. It was developed by Xu (2006) based on a combination of reflectance in the green band (Band 2 of Landsat TM/ETM+ image) and Short-Wave Infrared (SWIR) band (Band 5 of Landsat TM/ETM+ image). The mNDWI is calculated as

$$\mathrm{mNDWI} = \frac{\mathrm{Band\ 2} - \mathrm{Band\ 5}}{\mathrm{Band\ 2} + \mathrm{Band\ 5}} \tag{4}$$

The pixel values of mNDWI images derived from Landsat TM/ETM+ images using Eq. (4) range from −1 to 1. Pixels with mNDWI value greater than 0 generally represent water bodies. However, this threshold requires slight calibration for different images, where a manual adjustment of the threshold could always lead to more accurate results (Ji et al., 2009). The spatial distribution of inundated pixels on the mNDWI images was evaluated to determine the cut-off points to distinguish inundated extents. For each demonstration site, a Landsat TM/ETM+ image was selected and processed to mNDWI image using ENVI software. The selection of the TM/ETM+ image for each site was based on the maximum flow during the study period (water year 2001–2010) and the image availability. These images for evaluation were listed in Table 2.

MODIS derived inundation maps (Fig. 4(b) and (d)) and TM/ETM+ derived inundation maps (Fig. 5(b) and (d)) were resampled to 10 m using the nearest neighborhood method. Spatial comparisons were conducted based on these two groups of inundation maps (Fig. 6). Four indices were employed to indicate the delineation accuracy of MODIS OWL images against TM/ETM+ mNDWI images. They are overall accuracy, omission error, commission error and Kappa coefficient (Table 3). Overall accuracy is the percentage of total correctly classified pixels. Omission error represents the percentage of inundated pixels incorrectly classified as non-inundated pixels. Commission error is the percentage of non-inundated pixels classified as inundated pixels. Kappa coefficient is an index that estimates the agreement between two classifications taking into account the agreement occurring by chance. It is generally thought to be a more robust measure than the simple percentage agreement calculation. Kappa coefficient approaching 1 represents perfect agreement, with between 0.6 and 0.8 representing substantial agreement (Landis and Koch, 1977).

From Fig. 6, it can be seen that MODIS OWL images tend to miss isolated small patches of inundation or inundation in narrow channels. However, the overall shape and pattern of inundation seems to be reasonably well represented. As shown in Table 3, the overall accuracies of both the Narran site (97.0%) and the Chowilla site (94.8) are high. As the overall accuracy is a simple percentage between the correctly derived number of pixels (including both inundated and non-inundated) and the total number of pixels of the demonstration sites, the high accuracies are because of the large number of dry pixels and wet pixels of large water bodies. The Kappa coefficient considers the probability that a pixel is classified by chance, which therefore makes it more appropriate for evaluating detection accuracy. Both sites have Kappa coefficients around 0.6 which indicates an acceptable accuracy according to Landis and Koch (1977). The indices in Table 3 only represent the average evaluation result. In practice, the ability to detect inundation in MODIS products is largely limited by spectral confusion with background materials and depth of water, as well as the spatial inundation extent in relation to the pixel size.

3.4. Inundation mapping

Inundation mapping in this study is zone-based. For each zone, 10 peaks from the water years 2001 to 2010 were extracted from its related gauge using the annual flood series method. For each peak, inundation extent maps were derived from seven selected

Table 3
Evaluation results showing the accuracy of detection using MODIS imagery compared to Landsat TM/ETM+ images.

Demonstration site	Overall accuracy (%)	Omission error (%)	Commission error (%)	Kappa coefficient
Narran	97.0	2.1	0.9	0.6
Chowilla	94.8	3.0	2.2	0.6

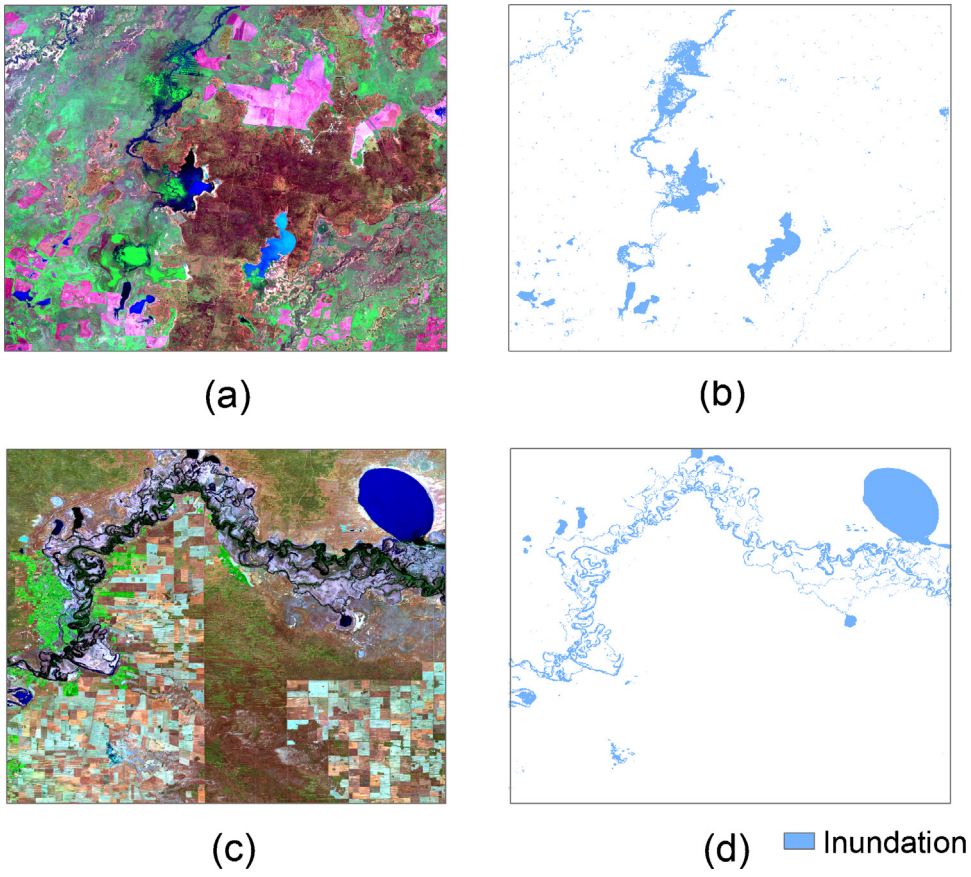

Fig. 5. (a) Color composite (R7G4B2) TM image (23/03/2010) of Narran Lakes; (b) inundation map with a threshold = −0.10 (mNDWI > −0.10) of Narran Lakes; (c) color composite (R7G4B2) ETM+ image (13/12/2000) of Chowilla; (d) inundation map with a threshold = −0.15 (mNDWI > −0.15) of Chowilla.

MODIS OWL images. They were then aggregated into one inundation extent map of which if any pixels were indicated to be inundated in any of the seven images, inundation was reported for this pixel. For each of the 10 water years, an annual maximum flood inundation map was created (Fig. 7).

These 10 annual maximum inundation maps were then overlaid to demonstrate the total number of years that areas were inundated throughout the 10 water years (Fig. 8). The number of times an area was inundated can be considered as the inundated frequency during this period.

Assuming that the inundation in each zone is closely correlated with the discharge from its related gauge, AEPs in Table 1 could be related with annual maximum inundation maps of zone 88 in Fig. 7. For instance, those pixels that were inundated in water year 2001 in zone 88 in Fig. 7 have a probability of 30.4% (Table 1) to be inundated in any one year in the future. Similarly, inundated

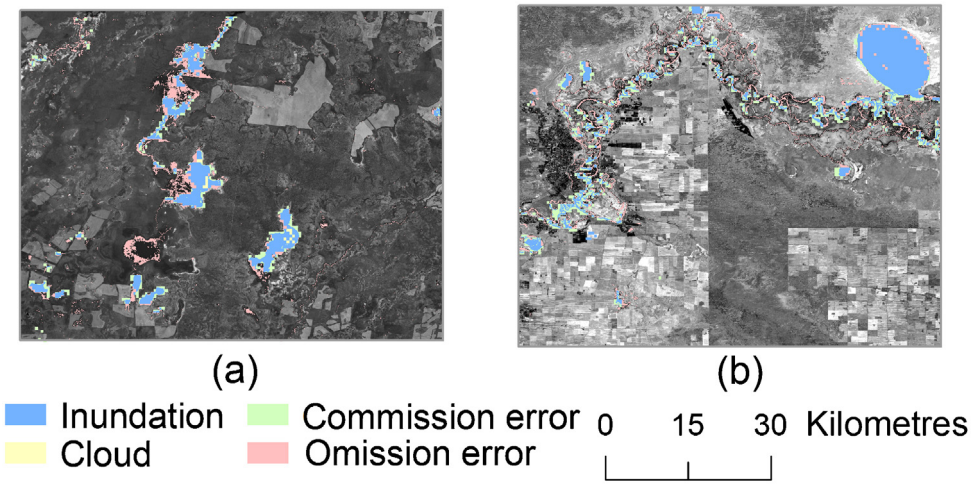

Fig. 6. Spatial evaluation for OWL inundation: (a) MODIS image (22/03/2010) *vs.* TM (23/03/2010) at Narran Lakes; (b) MODIS image (10/12/2000) *vs.* ETM+ (13/12/2000) at Chowilla.

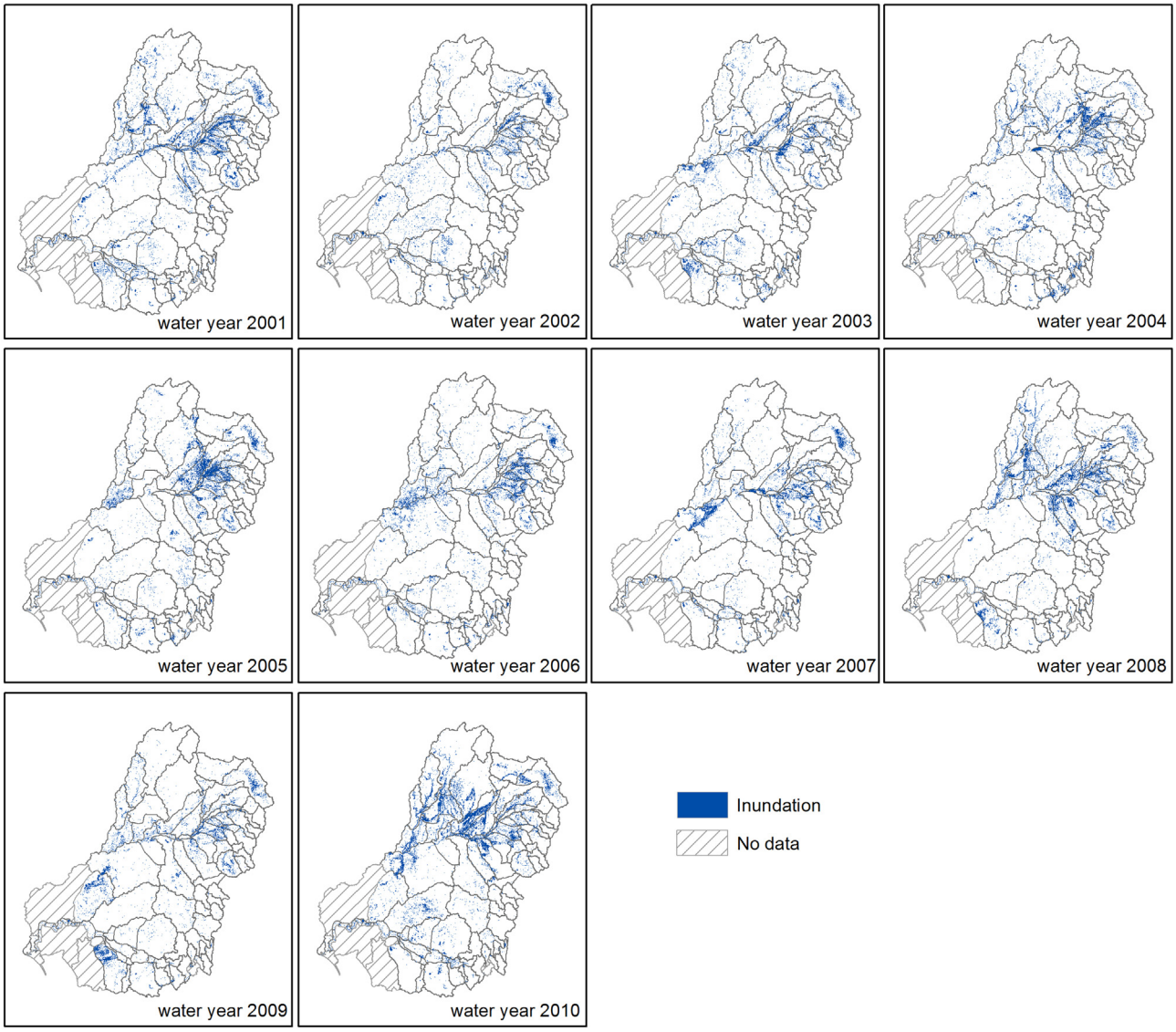

Fig. 7. Annual maximum inundation maps of the Basin showing the maximum inundation area of each water year between 2001 and 2010.

pixels in inundation maps of water year 2002–2010 also had their related probabilities. Therefore, corresponding to Fig. 7, 10 probability maps (year 2001–2010) were derived. These probability maps were then overlaid by taking the MAXIMUM probability to map the final inundation probability. As being derived from AEPs, inundation probability here is used as a reference to estimate the chance that an area could be inundated in any one year in the future, which is similar to the definition of AEP. As the AEP and the Average Recurrence Interval (ARI), which is commonly used in ecology when expressing an environmental water requirement (Chen et al., 2011), are similar metrics, Typical ARIs (1-in-1, 1-in-2...), therefore, can be adopted to represent the inundation probability. The relationship between AEP and ARI is defined by the following formula (Laurenson, 1987)

$$\mathrm{AEP} = 1 - \exp\left(\frac{-1}{\mathrm{ARI}}\right) \quad (5)$$

For those typical ARIs, their related AEPs are listed in Table 4. ARIs higher than 1-in-10 are very closely approximated by the reciprocal of AEPs (*e.g.* 1-in-20 represents 0.05 AEP). Considering this relationship, an inundation probability map was produced (Fig. 9).

Table 4
Conversion table between ARI and AEP.

ARI	1-in-1	1-in-2	1-in-5	1-in-10
AEP	0.632	0.393	0.181	0.095

4. Results and discussion

4.1. Inundation pattern

Across the MDB, the annual maximum inundation was highly variable with an area varying from 30,123 km^2 to 64,932 km^2 (Fig. 7). During the study period, the most widespread inundation was in water year 2010. The year with the smallest area of inundation was 2002.

As the annual maximum inundation maps were derived by linking the date with the flow peaks, the date of the inundation (as mapped in Fig. 7) can be considered to be the same as that of its related flow peak. Therefore, the seasonality of gauge data flow peaks was used to represent the seasonality of annual inundation in each zone. The Day Of Year (DOY) of those peaks among water year 2001–2010 were calculated based on their date, and mapped onto

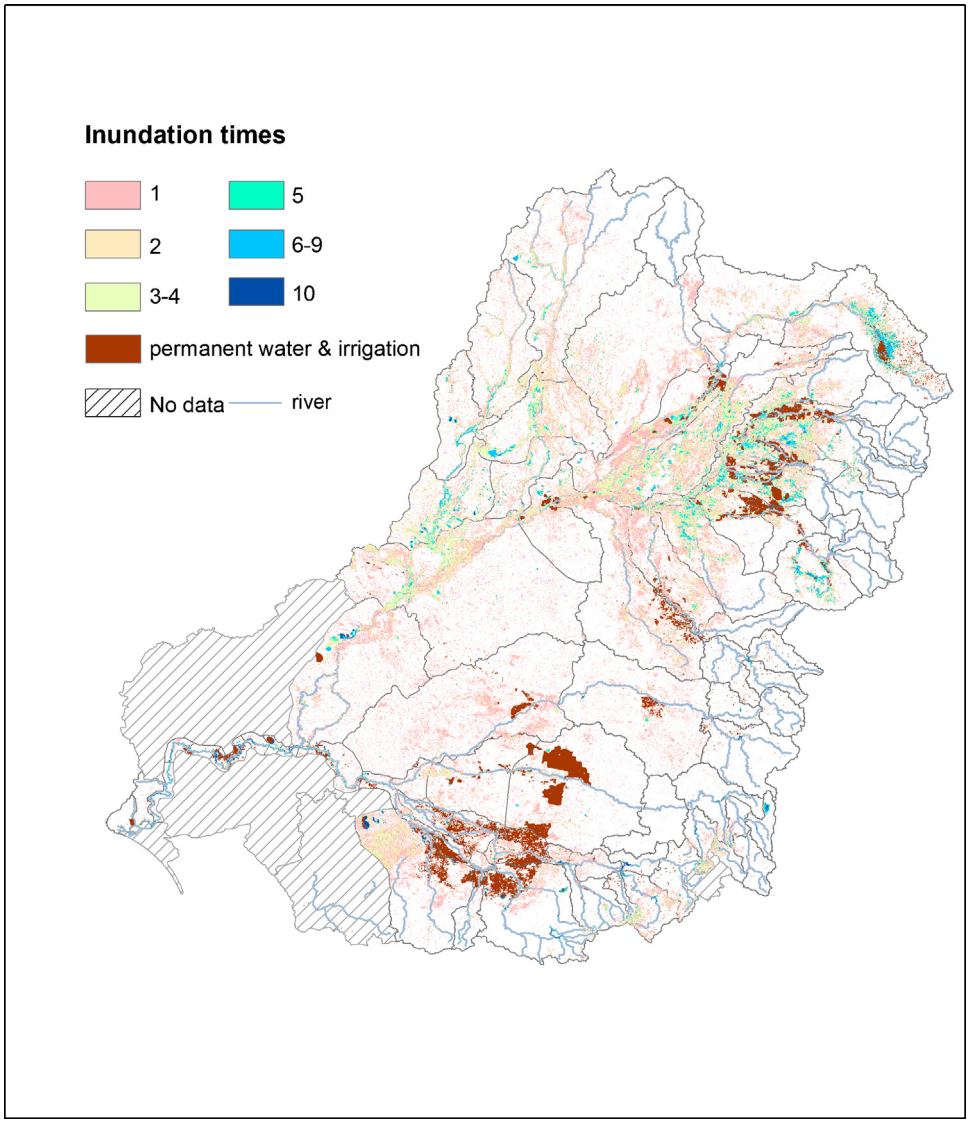

Fig. 8. Inundation frequency map developed from the inundated times over the water years 2001–2010.

the zones to indicate the seasons of their occurrence (Fig. 10). It can be identified that in most zones, discharge peaks usually occurred in spring or summer. However, water year 2006 and 2010 were exceptions, when many zones demonstrated peaks in winter and autumn respectively. After checking the flow peak DOY for each zone, those with winter flow peaks in water year 2006 largely had peaks which occurred in August, which is late winter, just prior to spring. The autumn flow peaks in water year 2010 generally occurred in March, during early autumn, closer to summer. The seasonality of flooding has a significant impact on the ecological response. For example, it is found that plant communities gained highest production and greatest expression during spring floods, nevertheless, wood production by river red gum (*Eucalyptus camaldulensis*) forests reaches its highest peak when receiving summer flood (Robertson et al., 2001). Therefore, this result has a guiding significance for studying the productivity of some biota.

4.2. Inundation frequency

Fig. 8 shows the inundation frequency over the period (water year 2001–2010). Obviously, high frequency areas are those that are near lakes or river channels. That is because floods in the Basin always begin from the high discharge of rivers.

The area of each inundation frequency (1–10 times in 10 years) in Fig. 8 was plotted as a percentage of total inundated area in the pie chart in Fig. 11. Excluding the permanent water bodies and irrigation areas, an area of 99,014 km^2 in total was inundated only once during these years, which is 55.3% of the total inundated area (179,150 km^2). An area of 1195 km^2 (about 0.7%) was inundated 10 times, which represents inundation at least once every year. Proportions of areas with different inundation frequencies in the north and south of the Basin were calculated and plotted as the bar chart in Fig. 11. Similarly in the north and south, area that was inundated only once in the 10 years had the biggest proportion (about 11.6% and 8.9%) of the total areas (623,618 km^2 of the north and 303,344 km^2 of the south). Inundation frequency in the southern part of the Basin was generally lower than that in the northern part. This could be because of the extensive river network in the north. The broad-distributed tributaries of the Darling River make the northern part easier to be inundated.

Inundation frequency describes how often the flood water submerged an area during the observed period. Flood water is an important water source for floodplain and wetland ecosystems, especially for those riparian plants, such as river red gum (Rogers and Ralph, 2010). Several studies indicated that healthy river red gum is suited in areas receiving adequate surface flooding (Bren

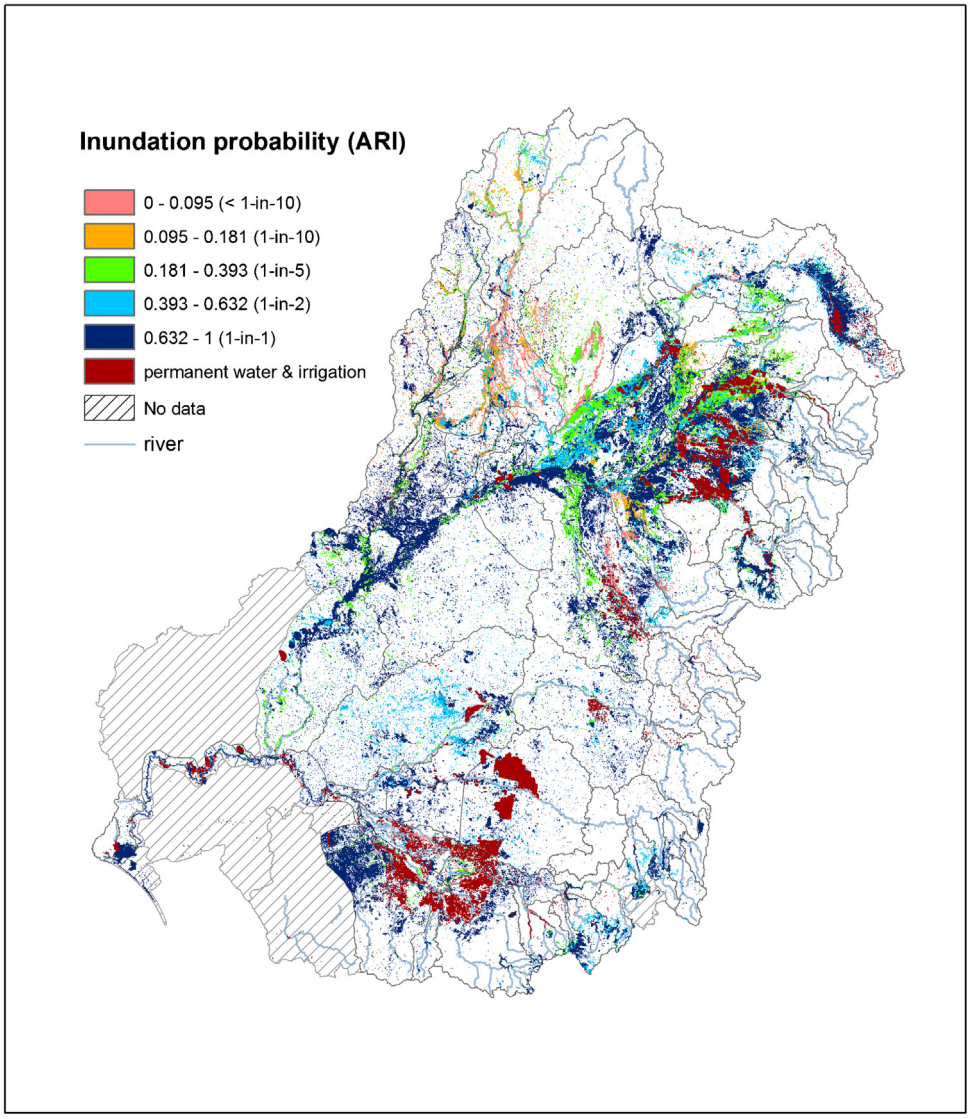

Fig. 9. Inundation probability map showing the probability of inundation in forms of typical ARIs.

and Gibbs, 1986; Robertson et al., 2001). Flood inundation associated with flood pulse also disperses seed and deposits fertile soil around roots of riparian plants, which is critical for their growth and reproduction. Inundation also provides opportunities for aquatic organisms to colonize a variety of habitats (Pringle, 2003). Some fish, for example, make use of floods to reach new habitats and gain prosperity. Therefore, flood inundation frequency is an important indicator for the well-being of riparian flora and fauna communities. The inundation frequency map and results can be a helpful support for ecosystem maintenance.

4.3. Inundation probability

The inundation probability map (Fig. 9) projects future inundation based on current flow data and MODIS images. Inundation probabilities are related to typical ARIs. It is generally assumed that the possible inundation extent associated with a less frequent ARI always includes the extent corresponding to a more frequent ARI. For example, 1-in-2 possible inundation extent includes the 1-in-1 possible inundation extent. Therefore, Fig. 9 was decomposed into four possible inundation maps related to four typical ARIs (Fig. 12). It can be seen that the inundation extent increases more slowly as the ARI rises. Separately, the possible inundation extent of these four ARIs in the south Basin is relatively less distributed than that in the north. The proportion of 1-in-1 possible inundation extent in the south Basin is 9.7%, while that in the north is much higher (14.1%). The same pattern exists in the possible inundation extents of the other typical ARIs (Fig. 12). The reason for this contrast between the north and south region is the same as that for the inundation frequency pattern, *i.e.* the wide-ranging tributaries of the Darling River make the northern part more likely to be inundated in the future.

Unlike the inundation frequency map which describes how often the flood water submerged an area historically, the inundation probability map gives an indicator of the future inundation frequency. It can be helpful when pre-formulating future possible flow regimes to ensure there is enough water for the important riparian ecosystems. For example, river red gum forests need to receive water from flood with 1-in-5 or more frequent ARI (Steenbeeke et al., 2000). As a result, their distribution should be included within the 1-in-5 possible inundation extent in Fig. 12. Once the distribution maps of river red gum and 1-in-5 possible inundation extent are overlaid, those river red gums that may not be able to receive enough flood water in the future can be easily

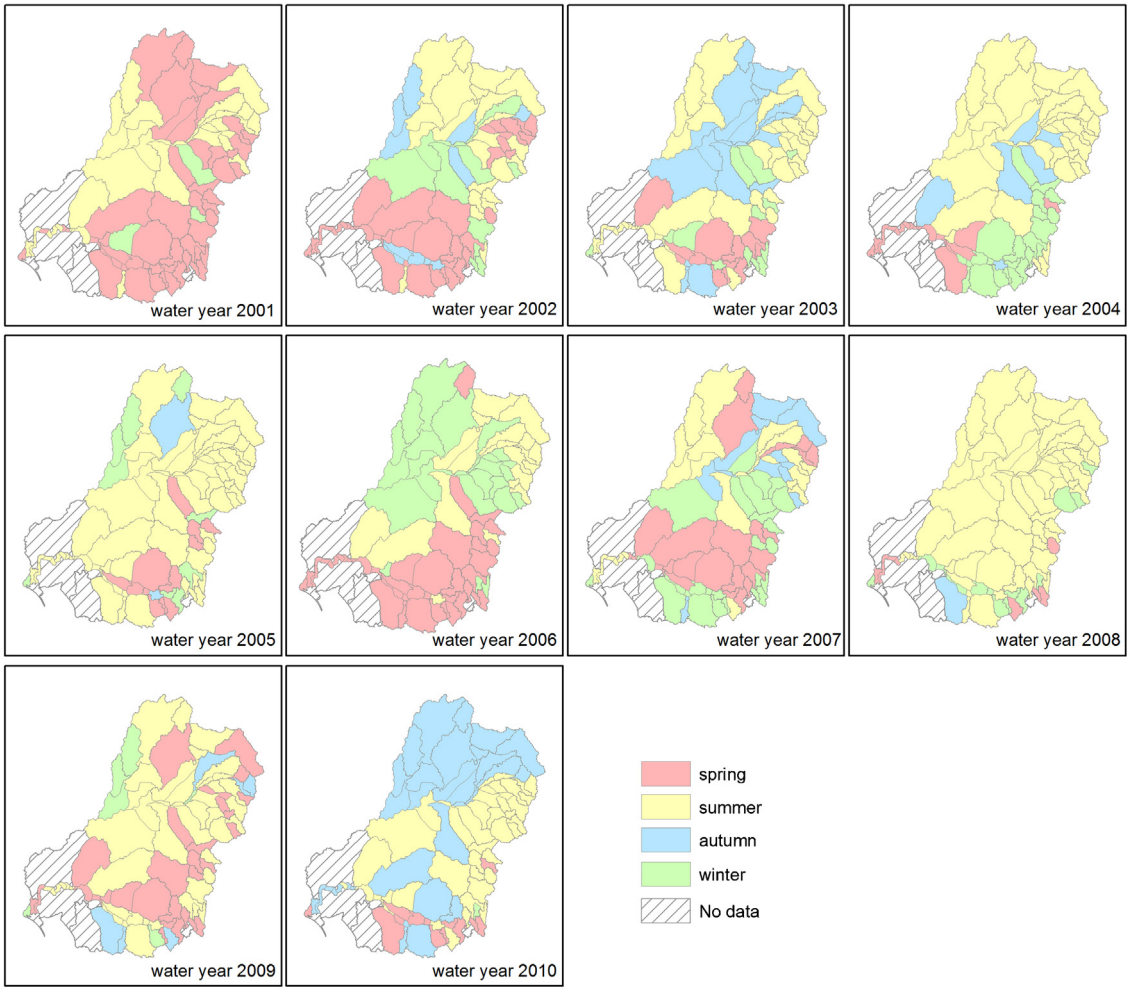

Fig. 10. Inundation seasonality maps developed from the date of flow peaks for each water year between 2001 and 2010.

identified. Thus, in order to protect them from degradation, serious consideration on environmental flow strategy needs to be implemented to make sure they receive adequate water.

It should be noted that, since the MODIS data covered a relatively dry period (from year 2001 to 2010), the inundation probability map generated in this study could potentially underestimate the probability of future inundation within the Basin. A longer time series of river flow and remotely sensed imagery will help capture more extreme flood events and hence allow for a more robust estimation of flood inundation probabilities.

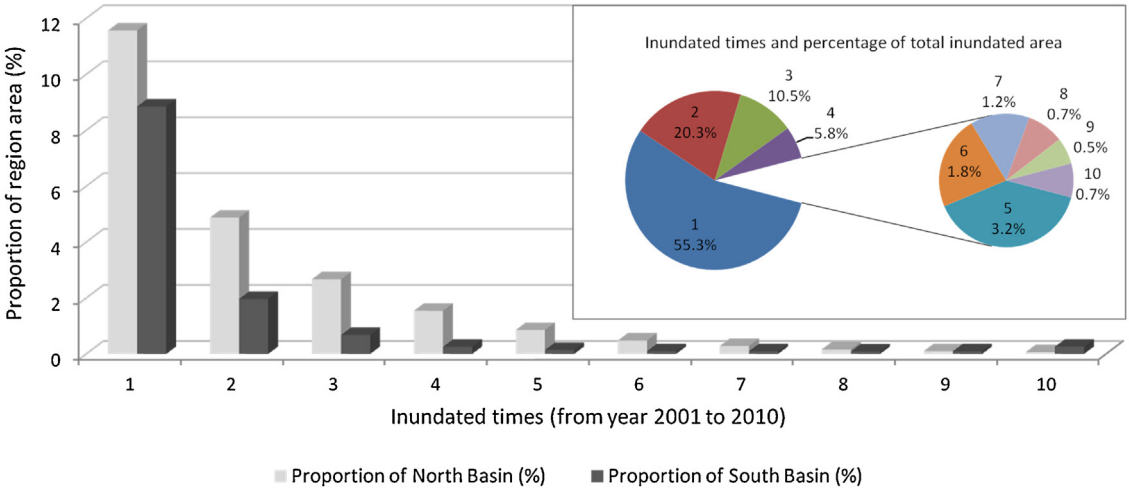

Fig. 11. Proportions of inundated area with different inundated times in north and south Basin (bar chart); percentage of different times based on the total inundated area in the Basin (pie chart).

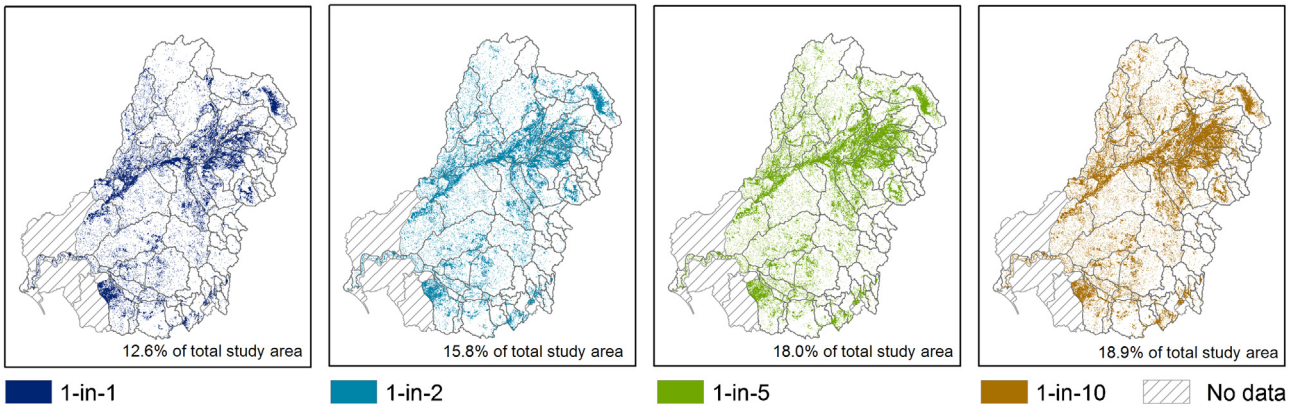

Fig. 12. Possible inundation extent maps of the Basin under four typical ARIs (1-in-1, 1-in-2, 1-in-5, 1-in-10).

5. Conclusions

A methodology for mapping spatial and temporal variations of flood inundation using observed flow data series and remotely sensed image series at basin scale was developed in this study. Observed gauge flow data were utilized to extract flow peaks and their AEPs using annual maximum series method. The flow peaks were then used to select appropriate MODIS images to detect flood inundation. Evaluation results demonstrated that inundation detected by OWL on MODIS images has an acceptable accuracy at basin scale, confirming the suitability of this technique for use in spatial and temporal mapping of flood inundation in large river basins. Detected inundation, in combination with flow peaks and AEPs, was exploited to map characteristics of flood inundation. Annual maximum inundation extent maps, flood inundation frequency map and inundation probability map were derived. The significance and implication of these inundation characteristic maps for ecological studies were highlighted. It is hoped that the methodology and resultant maps of this study will provide scientific basis for water resource management and wetland ecosystem researches.

This study integrates *in situ* observation data and remotely sensed data to map the characteristics of flood inundation over time and across large study areas. While the *in situ* hydrological data provide only point-based information, remote sensing data are helpful in transferring this information from point measurement to a large area. Linking hydrological data to remotely sensed inundation can produce spatio-temporal inundation maps with inherent hydrological characteristics, which will be useful to eco-hydrological studies in large river basins.

Acknowledgments

The authors want to thank the China Scholarship Council for providing a scholarship to Chang Huang to support this research at CSIRO Land and Water (CLW). This work was conducted under the auspices of the CLW and CSIRO's Water for a Healthy Country National Research Flagship. The authors are grateful to our colleagues: Linda Merrin, for her assistance on collecting flow data; Garth Warren and Dr. Juan Pablo Guerschman, for their help in downloading MODIS images and deriving OWL images; Susan Cuddy, Dr. Danial Stratford, Dave Penton and Dr. Catherine Ticehurst for reviewing the manuscript. The anonymous reviewers are acknowledged for their valuable comments.

References

Alsdorf, D.E., Lettenmaier, D.P., 2003. Tracking fresh water from space. Science 301, 1491–1494.

Alsdorf, D.E., Rodriguez, E., Lettenmaier, D.P., 2007. Measuring surface water from space. Rev. Geophys. 45, 1–24.

APFM, 2006. Environmental aspects of integrated flood management. Associated Programme on Flood Management, Geneva, Switzerland.

Bates, P.D., Horritt, M.S., Fewtrell, T.J., 2010. A simple inertial formulation of the shallow water equations for efficient two-dimensional flood inundation modelling. J. Hydrol. 387, 33–45.

Benke, A.C., Chaubey, I., Ward, G.M., Dunn, E.L., 2000. Flood pulse dynamics of an unregulated river floodplain in the southeastern US coastal plain. Ecology 81, 2730–2741.

Bhavsar, P.D., 1984. Review of remote sensing applications in hydrology and water resources management in India. Adv. Space Res. 4, 193–200.

Blasco, F., Bellan, M.F., Chaudhury, M.U., 1992. Estimating the extent of floods in bangladesh using SPOT data. Remote Sens. Environ. 39, 167–178.

Brakenridge, G.R., 2013. Global Active Archive of Large Flood Events. Dartmouth Flood Observatory, University of Colorado, http://floodobservatory.colorado.edu/index.html [accessed on 30/3/2013].

Bren, L.J., Gibbs, N.L., 1986. Relationship between flood frequency, vegetation and topography in a river red gum forest. Aust. For. Res. 16, 357–370.

Chen, Y., Cuddy, S.M., Merrin, L.E., Huang, C., Pollock, D., Sims, N., Wang, B., Bai, Q., 2012a. Murray-Darling Basin Floodplain Inundation Model Version 2. 0 (MDB-FIM2). CSIRO Water for a Healthy Country Flagship, Canberra, Australia.

Chen, Y., Cuddy, S.M., Wang, B., Merrin, L.E., Pollock, D., Sims, N., 2011. Linking inundation timing and extent to ecological response models using the Murray-Darling Basin Floodplain Inundation Model (MDB-FIM). In: Proceedings of 19th International Congress on Modelling and Simulation, Perth, Austalia.

Chen, Y., Huang, C., Ticehurst, C., Merrin, L., Thew, P., 2013. An evaluation of MODIS daily and 8-day composite products for floodplain and wetland inundation mapping. Wetlands 33, 823–835.

Chen, Y., Wang, B., Pollino, C.A., Merrin, L.E., 2012b. Spatial modelling of potential soil water retention under floodplain inundation using remote sensing and GIS. In: Proceedings of 2012 International Congress on Environmental Modelling and Software, Leipzig, Germany.

CSIRO, 2008. Water Availability in the Murray-Darling Basin. A report to the Australian Government from the CSIRO Murray-Darling Basin Sustainable Yields Project , Canberra, Australia.

Cunnane, C., 1978. Unbiased plotting positions — a review. J. Hydrol. 37, 205–222.

Di Baldassarre, G., Schumann, G., Brandimarte, L., Bates, P., 2011. Timely low resolution SAR imagery to support floodplain modelling: a case study review. Surv. Geophys. 32, 255–269.

Dutta, D., Alam, J., Umeda, K., Hayashi, M., Hironaka, S., 2007. A two-dimensional hydrodynamic model for flood inundation simulation: a case study in the lower Mekong river basin. Hydrol. Process. 21, 1223–1237.

Frank, E., Ostan, A., Coccato, M., Stelling, G.S., 2001. Use of an integrated one dimensional-two dimensional hydraulic modelling approach for flood hazard and risk mapping. In: Proceedings of 1st International Conference on River Basin Management, Cardiff, Wales.

Frazier, P., Page, K., 2009. A reach-scale remote sensing technique to relate wetland inundation to river flow. River Res. Appl. 25, 836–849.

Frazier, P., Page, K., Louis, J., Briggs, S., Robertson, A.I., 2003. Relating wetland inundation to river flow using Landsat TM data. Int. J. Remote Sens. 24, 3755–3770.

Gallant, J.C., Dowling, T.I., 2003. A multiresolution index of valley bottom flatness for mapping depositional areas. Water Resour. Res. 39, 1347–1360.

Gao, B.C., 1996. NDWI – a normalized difference water index for remote sensing of vegetation liquid water from space. Remote Sens. Environ. 58, 257–266.

Garcia-Pintado, J., Neal, J.C., Mason, D.D., Dance, S.L., Bates, P.D., 2013. Scheduling satellite-based SAR acquisition for sequential assimilation of water level observations into flood modelling. J. Hydrol. 495, 252–266.

Giustarini, L., Matgen, P., Hostache, R., Montanari, M., Plaza, D., Pauwels, V.R.N., De Lannoy, G.J.M., Keyser, R., Pfister, L., Hoffmann, L., Savenije, H.H.G., 2011. Assimilating SAR-derived water level data into a hydraulic model: a case study. Hydrol. Earth Syst. Sci. 15, 2349–2365.

Gringorten, I.I., 1963. A plotting rule for extreme probability paper. J. Geophys. Res. 68, 813–814.
Guerschman, J.P., Warren, G., Byrne, G., Lymburner, L., Mueller, N., Van Dijk, A., 2011. MODIS-based Standing Water Detection for Flood and Large Reservoir Mapping: Algorithm Development and Applications for the Australian Continent. CSIRO, Canberra, Australia.
Gumbricht, T., Wolski, P., Frost, P., McCarthy, T.S., 2004. Forecasting the spatial extent of the annual flood in the Okavango delta, Botswana. J. Hydrol. 290, 178–191.
Guo, S.L., 1990. A discussion on unbiased plotting positions for the general extreme value distribution. J. Hydrol. 121, 33–44.
Huang, C., Chen, Y., Wu, J., 2013. A DEM-based modified pixel swapping algorithm for floodplain inundation mapping at subpixel scale. In: Proceedings of 2013 IEEE International Geoscience and Remote Sensing Symposium (IGARSS2013), Melbourne, Australia.
Huang, C., Chen, Y., Wu, J., Yu, J., 2012a. Detecting floodplain inundation frequency using MODIS time-series imagery. In: Proceedings of 2012 First International Conference on Agro-Geoinformatics, Shanghai, China.
Huang, S.F., Li, J.G., Xu, M., 2012b. Water surface variations monitoring and flood hazard analysis in Dongting Lake area using long-term Terra/MODIS data time series. Nat. Hazards 62, 93–100.
Hui, F.M., Xu, B., Huang, H.B., Yu, Q., Gong, P., 2008. Modelling spatial-temporal change of Poyang Lake using multitemporal Landsat imagery. Int. J. Remote Sens. 29, 5767–5784.
Islam, A.S., Bala, S.K., Haque, M.A., 2010. Flood inundation map of Bangladesh using MODIS time-series images. J. Flood Risk Manage. 3, 210–222.
Islam, M.M., Sado, K., 2000a. Development of flood hazard maps of Bangladesh using NOAA-AVHRR images with GIS. Hydrol. Sci. J. 45, 337–355.
Islam, M.M., Sado, K., 2000b. Flood hazard assessment in Bangladesh using NOAA AVHRR data with geographical information system. Hydrol. Process. 14, 605–620.
Ji, L., Zhang, L., Wylie, B., 2009. Analysis of dynamic thresholds for the normalized difference water index. Photogramm. Eng. Remote Sens. 75, 1307–1317.
Kim, S., Shin, H., Joo, K., Heo, J.H., 2012. Development of plotting position for the general extreme value distribution. J. Hydrol. 475, 259–269.
Kingsford, R.T., Brandis, K., Thomas, R.F., Crighton, P., Knowles, E., Gale, E., 2004. Classifying landform at broad spatial scales: the distribution and conservation of wetlands in New South Wales, Australia. Mar. Freshw. Res. 55, 17–31.
Kwak, Y., Park, J., Fukami, K., 2011. Nation-wide flood risk assessment using inundation level model and MODIS time-series imagery. In: Proceedings of 2011 IEEE International Geoscience and Remote Sensing Symposium (IGARSS 2011), Vancouver, Canada.
Landis, J.R., Koch, G.G., 1977. The measurement of observer agreement for categorical data. Biometrics 33, 159–174.
Laurenson, E.M., 1987. Back to basics on flood frequency analysis. Trans. Inst. Eng. Aust. Civ. Eng. 29, 47–53.
Li, B., Yan, Q., Zhang, L., 2011. Flood monitoring and analysis over the middle reaches of Yangtze river basin using MODIS time-series imagery. In: Proceedings of 2011 IEEE International Geoscience and Remote Sensing Symposium (IGARSS 2011), Vancouver, BC.
Mason, D.C., Schumann, G.J.P., Neal, J.C., Garcia-Pintado, J., Bates, P.D., 2012. Automatic near real-time selection of flood water levels from high resolution synthetic aperture radar images for assimilation into hydraulic models: a case study. Remote Sens. Environ. 124, 705–716.
Matgen, P., Schumann, G., Henry, J.B., Hoffmann, L., Pfister, L., 2007. Integration of SAR-derived river inundation areas, high-precision topographic data and a river flow model toward near real-time flood management. Int. J. Appl. Earth Obs. 9, 247–263.
McFeeters, S.K., 1996. The use of the normalized difference water index (NDWI) in the delineation of open water features. Int. J. Remote Sens. 17, 1425–1432.
Michishita, R., Gong, P., Xu, B., 2012. Spectral mixture analysis for bi-sensor wetland mapping using Landsat TM and Terra MODIS data. Int. J. Remote Sens. 33, 3373–3401.
Neal, J.C., Schumann, G.J.P., Bates, P., 2012. A subgrid channel model for simulating river hydraulics and floodplain inundation over large and data sparse areas. Water Resour. Res. 48, W11506.
Ordoyne, C., Friedl, M.A., 2008. Using MODIS data to characterize seasonal inundation patterns in the Florida everglades. Remote Sens. Environ. 112, 4107–4119.
Overton, I.C., 2005. Modelling floodplain inundation on a regulated river: Integrating GIS, remote sensing and hydrological models. River Res. Appl. 21, 991–1001.
Overton, I.C., Colloff, M.J., Doody, T.M., Henderson, B., Cuddy, S.M., 2009. Ecological Outcomes of Flow Regimes in the Murray-Darling Basin. Water for a Healthy Country Flagship. CSIRO, Adelaide, Australia.
Overton, I.C., Doody, T.M., Chen, Y., Pollock, D., Sims, N., 2011. Murray-Darling Basin Floodplain Inundation Model (MDB-FIM). Water for a Healthy Country Flagship. CSIRO, Adelaide, Australia.
Page, K.J., McElroy, L., 1981. Comparison of Annual and Partial Duration Series Floods on the Murrumbidgee River. Water Resour. Bull. 17, 286–289.
Papa, F., Prigent, C., Rossow, W.B., 2008. Monitoring flood and discharge variations in the large siberian rivers from a multi-satellite technique. Surv. Geophys. 29, 297–317.
Pappenberger, F., Dutra, E., Wetterhall, F., Cloke, H.L., 2012. Deriving global flood hazard maps of fluvial floods through a physical model cascade. Hydrol. Earth. Syst. Sci. 16, 4143–4156.
Paz, A.R., Collischonm, W., Tucci, C.E.M., Padovani, C.R., 2011. Large-scale modelling of channel flow and floodplain inundation dynamics and its application to the Pantanal (Brazil). Hydrol. Process. 25, 1498–1516.
Pringle, C., 2003. What is hydrologic connectivity and why is it ecologically important? Hydrol. Process. 17, 2685–2689.
Pulvirenti, L., Chini, M., Pierdicca, N., Guerriero, L., Ferrazzoli, P., 2011. Flood monitoring using multi-temporal COSMO-SkyMed data: Image segmentation and signature interpretation. Remote Sens. Environ. 115, 990–1002.
Rango, A., Salomonson, V.V., 1974. Regional flood mapping from space. Water Resour. Res. 10, 473–484.
Robertson, A.I., Bacon, P., Heagney, G., 2001. The responses of floodplain primary production to flood frequency and timing. J. Appl. Ecol. 38, 126–136.
Rogers, K., Ralph, J.T., 2010. Floodplain Wetland Biota in the Murray-Darling Basin: Water and Habitat Requirements. CSIRO Publishing, Collingwood, Victoria, Australia.
Saf, B., 2009. Regional flood frequency analysis using L moments for the Buyuk and Kucuk Menderes river basins of Turkey. J. Hydrol. Eng. 14, 783–794.
Sakamoto, T., Van Nguyen, N., Kotera, A., Ohno, H., Ishitsuka, N., Yokozawa, M., 2007. Detecting temporal changes in the extent of annual flooding within the Cambodia and the Vietnamese Mekong Delta from MODIS time-series imagery. Remote Sens. Environ. 109, 295–313.
Seckin, N., Haktanir, T., Yurtal, R., 2011. Flood frequency analysis of Turkey using L-moments method. Hydrol. Process. 25, 3499–3505.
Shi, P., Chen, X., Qu, S.M., Zhang, Z.C., Ma, J.L., 2010. Regional frequency analysis of low flow based on L moments: case study in Karst area, Southwest China. J. Hydrol. Eng. 15, 370–377.
Smith, L.C., 1997. Satellite remote sensing of river inundation area, stage, and discharge: a review. Hydrol. Process. 11, 1427–1439.
Smith, L.C., Isacks, B.L., Bloom, A.L., Murray, A.B., 1996. Estimation of discharge from three braided rivers using synthetic aperture radar satellite imagery: potential application to ungaged basins. Water Resour. Res. 32, 2021–2034.
Steenbeeke, G., Kidson, R., Witts, T., Brereton, G., 2000. A review of recent studies investigating biological & physical processes in the Macquarie Marshes. Riverine Environment Unit, Central West Region, NSW Department of Land and Water Conservation, New South Wales, Australia.
Thomas, R.F., Kingsford, R.T., Lu, Y., Hunter, S.J., 2011. Landsat mapping of annual inundation (1979–2006) of the Macquarie Marshes in semi-arid Australia. Int. J. Remote Sens. 32, 4545–4569.
Thoms, M.C., Sheldon, F., 2000. Water resource development and hydrological change in a large dryland river: the Barwon-Darling river, Australia. J. Hydrol. 228, 10–21.
Townshend, J.R.G., Justice, C.O., 1986. Analysis of the dynamics of african vegetation using the normalized difference vegetation index. Int. J. Remote Sens. 7, 1435–1445.
USGS, 2011. U.S. Geological Survey's Earth Resources Observation and Science (EROS) Center. http://eros.usgs.gov/ [accessed on 23.04.12].
USGS, 2012. NASA Land Processes Distributed Active Archive Centre (LP DAAC). https://lpdaac.usgs.gov/products/modis_products_table/mod09a1 [accessed on 23.04.12].
Vorosmarty, C.J., Willmott, C.J., Choudhury, B.J., Schloss, A.L., Stearns, T.K., Robeson, S.M., Dorman, T.J., 1996. Analyzing the discharge regime of a large tropical river through remote sensing, ground-based climatic data, and modeling. Water Resour. Res. 32, 3137–3150.
Wang, Y., Colby, J.D., Mulcahy, K.A., 2002. An efficient method for mapping flood extent in a coastal floodplain using Landsat TM and DEM data. Int. J. Remote Sens. 23, 3681–3696.
Ward, J.V., Tockner, K., Arscott, D.B., Claret, C., 2002. Riverine landscape diversity. Freshw. Biol. 47, 517–539.
Westerhoff, R.S., Kleuskens, M.P.H., Winsemius, H.C., Huizinga, H.J., Brakenridge, G.R., Bishop, C., 2013. Automated global water mapping based on wide-swath orbital synthetic-aperture radar. Hydrol. Earth Syst. Sci. 17, 651–663.
Westra, T., De Wulf, R.R., 2009. Modelling yearly flooding extent of the Waza-Logone floodplain in northern Cameroon based on MODIS and rainfall data. Int. J. Remote Sens. 30, 5527–5548.
Wilson, M., Bates, P.D., Alsdorf, D., Forsberg, B., Horritt, M., Melack, J., Frappart, F., Famiglietti, J., 2007. Modeling large-scale inundation of Amazonian seasonally flooded wetlands. Geophys. Res. Lett. 34, L15404.
Yamazaki, D., Kanae, S., Kim, H., Oki, T., 2011. A physically based description of floodplain inundation dynamics in a global river routing model. Water Resour. Res. 47, W04501.
Xu, H.Q., 2006. Modification of normalised difference water index (NDWI) to enhance open water features in remotely sensed imagery. Int. J. Remote Sens. 27, 3025–3033.